Researchers Journal of Science and Technology (REJOST)
https://rejost.com.ng

Dose-Dependent Irradiation Effects on Lithium–Air Battery Performance

S. O. Akintunde* and D. O. Kehinde

Abstract

The effect of irradiation dose on the performance of lithium–air batteries was investigated using a coupled electrochemical–defect evolution model. The model describes oxygen and lithium transport, lithium peroxide precipitation, and Butler–Volmer electrochemical kinetics. Irradiation-induced defects are treated as a dynamic variable that modifies diffusivity, exchange current density, and specific surface area through a biphasic mechanism. Numerical simulations were performed under control, low-dose, medium-dose, and high-dose conditions to characterize the full dose-dependent behaviour. The results reveal a nonlinear response. In the control case, current, power, and capacity remain minimal due to slow electrochemical kinetics. Low-dose irradiation enhances reaction activity while preserving transport. This produces modest increases in peak current and power and dramatic gains in capacity and energy that increase by more than 1500% relative to control. Medium and high doses generate sharp current and power spikes, but these are not sustained. In such cases, lithium peroxide formation collapses, capacity and energy drop to nearly zero, and the electrolyte potential diverges as defect densities exceed 10^{22} m^{-3}. The study establishes irradiation as a double-edged influence on lithium–air batteries. At low doses, defects improve kinetics and product formation within an optimal defect window. At higher doses, excessive defects suppress transport and lead to performance failure. The novelty of this work lies in unifying irradiation physics with lithium–air battery modeling, to our knowledge, a biphasic window has not been reported in the Li–air literature. This provides new theoretical insight and practical guidance for the design of irradiation-assisted energy storage systems.

✉ S. O. Akintunde: akintundes@babcock.edu.ng
Department of Basic Sciences, Babcock University, Ilishan-Remo, Ogun State

Keywords: Lithium–air batteries, Irradiation effects, Defect dynamics, Electrochemical performance, Dose-dependent enhancement

Article history

Received: July 28, 2025
Received in revised form: September 26, 2925
Accepted for publication: October 2, 2025
Available online: October 4, 2025

1.0 Introduction

Lithium–air batteries (LABs) have attracted significant attention because of their extremely high theoretical energy density (Zaidi and Li, 2023; Liu *et al*., 2020). Their gravimetric energy density can exceed 3000 Wh kg^{-1}, which is nearly ten times higher than that of current lithium-ion batteries (Amine *et al*., 2014; Imanishi *et al*., 2014; Akhtar, 2015). This advantage makes LABs strong candidates for applications such as electric vehicles, aerospace, and grid-scale storage (Khan *et al*., 2025; Lampic *et al*., 2016; Bugga *et al*., 2007). In principle, the open system design of the lithium–air battery, which uses oxygen from the environment as a reactant, provides a lightweight and energy-dense alternative to conventional batteries (Rahman *et al*., 2013; Guo *et al*., 2024).

Despite this promise, the practical realization of LABs remains very difficult. The oxygen reduction and oxygen evolution reactions (ORR and OER) that occur at the cathode are extremely slow. Large overpotentials are required to drive these reactions, which lowers energy efficiency. In addition, the formation of lithium peroxide, Li_2O_2, during discharge clogs the porous cathode, blocks active sites, and reduces cyclability (Huang *et al.*, 2025). Electrolytes also suffer from decomposition under reactive oxygen species, further limiting stability (Tan *et al*., 2016; Yu *et al*., 2025). Many approaches have been proposed to address these barriers. Catalysts such as transition metals and oxides have been developed to accelerate kinetics (Lüchtefeld *et al.*, 2023). Alternative electrolytes have been tested to improve chemical stability (Liu *et al*., 2022). Cathode architectures have been redesigned to maximize pore volume and maintain conductivity (He *et al*., 2024; Numan-Al-Mobin *et al*., 2022). While progress has been achieved, these approaches have not yet resolved the core limitations, and the gap between theoretical and practical energy density remains large.

In parallel, irradiation has become an important tool for engineering the properties of materials. When high-energy particles or radiation interact with solids, they create a variety of defects, including vacancies, interstitials, and dislocation loops (Akintunde and Selyshchev, 2016; [a]Akintunde *et al*., 2025; [b]Akintunde *et al*., 2025). These defects strongly influence transport, reactivity, and structural stability (Was, 2007). Irradiation can alter diffusion pathways, change electrical conductivity, and modify surface chemistry (Zhang *et al*., 2018; Fan, 2025). It can also restructure interfaces or destabilize microstructures depending on dose and particle energy (Chowdhury, 2022). This sensitivity makes irradiation a versatile but complex tool in materials science.

Applications of irradiation in electrochemical systems have also been explored. In lithium-ion batteries, irradiation has been reported to modify impedance and affect cycle stability (Gao *et al*., 2023; Qiu *et al*., 2015). In solid electrolytes, irradiation can either enhance or suppress ionic transport depending on defect concentration and type (Mbayachi, 2025; Kulathuvayal and Su, 2023). These findings indicate that irradiation has the potential to reshape the performance of energy storage systems. However, lithium–air batteries remain largely unexamined in this context. Their dependence on oxygen transport and precipitation reactions makes them especially sensitive to microstructural and transport changes. The absence of studies that connect irradiation to LAB operation therefore represents an important gap in the literature.

The goal of this research is to address that gap. This work investigates how irradiation dose influences the electrochemical performance of lithium–air batteries. The study focuses on the relationship between defect density and key performance metrics. These include peak current, peak power, discharge capacity, and total energy. It also examines lithium peroxide deposition profiles, electrolyte potential, and the evolution of defect density. Together, these

provide a mechanistic picture of dose-dependent behaviour in LABs.

The novelty of this study lies in its integration of irradiation physics with lithium–air battery modeling. Previous works have examined irradiation in structural alloys, nuclear materials, and lithium-ion systems. Other studies have investigated kinetics, mass transport, and precipitation in LABs. To the best of our knowledge, no study has combined these areas into a single framework. This study connects the two fields and shows how irradiation alters LAB performance through defect-driven processes. It also identifies the ranges where these effects become significant. In this way, the work adds a new dimension to the design and optimization of lithium–air batteries.

2.0 Materials and Methods

2.1 Theoretical Model

The performance of lithium–air batteries under irradiation is governed by coupled electrochemical reactions and defect dynamics within the electrode and electrolyte. The system is modeled as a one-dimensional porous cathode, where oxygen transport, lithium-ion diffusion, lithium peroxide formation, and defect evolution occur simultaneously. Irradiation introduces additional defects that modify reaction kinetics and transport properties in a dose-dependent manner.

The oxygen transport within the cathode is described by a diffusion equation with spatially varying diffusivity, $Do_2(x, t)$ [$m^2.s^{-1}$], to account for defect-mediated changes:

$$\frac{\partial Co_2}{\partial t} = \frac{\partial}{\partial x}\left(D_{O_2}(x,t)\frac{\partial Co_2}{\partial x}\right) - R_{rnx}(x,t) \quad (1)$$

Here, Co_2 is the local oxygen concentration in [$mol.m^{-3}$]. The first term on the right-hand side represents diffusion through the porous cathode, and the second term, R_{rnx} [$mol.m^{-3}.s^{-1}$], represents the rate of oxygen consumption due to electrochemical and chemical reactions. The spatial dependence of Do_2 accounts for the fact that irradiation-induced defects can locally hinder oxygen mobility.

Lithium-ion transport is similarly described by a diffusion equation:

$$\frac{\partial C_{Li}}{\partial t} = D_{Li}\frac{\partial^2 C_{Li}}{\partial x^2} - R_{chem}(x, t) \quad (2)$$

where C_{Li} [$mol.m^{-3}$] is the lithium-ion concentration and R_{chem} [$mol.m^{-3}.s^{-1}$], represents consumption by chemical side reactions, including lithium peroxide formation. D_{Li} [$m^2.s^{-1}$] may be treated as constant or weakly dependent on defect density for simplicity in eq. (2).

Lithium peroxide formation, Li_2O_2, results from the coupling of lithium ions and oxygen at the cathode surface. Its accumulation is governed by:

$$\frac{\partial C_{Li_2O_2}}{\partial t} = \frac{1}{2}R_{precip}(x, t) \quad (3)$$

where R_{precip} [$mol.m^{-3}.\ s^{-1}$] represents the local precipitation rate of Li_2O_2. The factor $\frac{1}{2}$ arises from the stoichiometry of Li_2O_2 formation from lithium and oxygen. The rate of precipitation depends on the local supersaturation of lithium and oxygen and is modified by the specific surface area of reaction sites, $a_s(x,t)$ [m^{-1}], which is itself enhanced under low irradiation doses and suppressed under high doses.

The precipitation kinetics were explicitly modeled using the rate law:

$$R_{precip} = k_p a_s(x,t)\left(\frac{C}{C_{sat}} - 1\right)^n$$

where k_p [m/s] is the precipitation rate constant, $\frac{C}{C_{sat}}$ is the local supersaturation ratio, and n is an empirical exponent describing the sensitivity of precipitation to supersaturation.

In our simulations, representative values of k_p = 1.0 × 10^{-5} m/s and n = 2 were used for Li_2O_2 nucleation and growth kinetics. The specific surface area $a_s(x,t)$ is dynamically modified by irradiation, being enhanced under low irradiation doses and suppressed under high doses.

Under the conditions studied, precipitation is primarily diffusion-limited due to oxygen transport through the cathode. Surface-reaction contributions are also included to explain reaction-limited behaviour at low overpotentials. Because direct experimental data for k_p and n under irradiation conditions are not available, these parameters are treated as modeling inputs. Their values are chosen to ensure that the system explores both diffusion-limited and reaction-limited regimes. The electrochemical reaction at the cathode is described using the full Butler–Volmer formulation:

$$i(x,t) = i_0(x,t)\left[\exp\left(\frac{\alpha_a F\eta(x,t)}{RT}\right) - \exp\left(\frac{-\alpha_c F\eta(x,t)}{RT}\right)\right] \quad (4)$$

Here, $i_0(x,t)$ [A.m^{-2}] is the exchange current density at position x, modified by the biphasic enhancement factor due to irradiation. $\eta(x,t)$ [V] is the local overpotential, F [96485 C.mol^{-1}] is Faraday's constant, R [8.314 J.mol^{-1}. K^{-1}] is the universal gas constant, and T [K] is the absolute temperature. α_a and α_c are the anodic and cathodic transfer coefficients, respectively. This expression describes the nonlinear voltage–current relationship that dominates battery performance.

The local overpotential is defined as:

$$\phi_s(x,t) - \phi_e(x,t) - U_{eq}\left(C_{O_2}, C_{Li}\right) \quad (5)$$

where ϕ_s and ϕ_e [V] are the local potentials of the solid electrode and electrolyte, respectively. U_{eq} [V] is the equilibrium potential of the oxygen reduction reaction, which depends on local concentrations of reactants. This self-consistent potential framework ensures that both electronic and ionic transport limitations are considered.

Irradiation introduces a dynamic defect density, $n_D(x,t)$ [m^{-3}], which evolves according to a source term proportional to the irradiation dose rate, G [$m^{-3}.s^{-1}$], and recombination or annihilation processes:

$$\frac{\partial n_D}{\partial t} = G - k_{rec} n_D + D_D \frac{\partial^2 n_D}{\partial x^2} \quad (6)$$

Here, k_{rec} [s^{-1}] is the recombination coefficient of defects, and D_D [$m^2.s^{-1}$] represents defect diffusivity. The local defect density affects both diffusivity and the specific reaction surface area:

$$D_{O_2}(x,t) = D_{O_2,0}\exp\left[-\beta\left(\frac{n_D(x,t)}{n_{D,0}} - 1\right)\right] \quad (7)$$

$$a_s(x,t) = a_{s,0}\left[1 + A_{enh}\frac{n_D(x,t)}{n_{D,0}}\exp\left(-\frac{n_D(x,t)}{n_{D,max}}\right)\right] \quad (8)$$

Here, $Do_{2,0}$ is the reference oxygen diffusivity in the porous cathode in the absence of irradiation-induced defects. It sets the baseline level of oxygen mobility under control conditions. The parameter β is the suppression factor. It measures the sensitivity of oxygen diffusivity to irradiation-induced defects. $a_{s,0}$ is the reference specific surface area of the cathode in the absence of irradiation-induced defects. A_{enh} is the enhancement amplitude, which determines how strongly the surface area increases at moderate defect densities. $n_{D,0}$ is the reference defect density, used as a scaling factor to normalize the actual defect density, n_D (x, t). Equation (7) shows the exponential decrease of diffusivity with defect density, while eq. (8) represents the biphasic enhancement of the specific surface area, where moderate defect densities increase electrochemical activity, but

excessive defects suppress it. The local current density, integrated over the electrode thickness, gives the total current output:

$$I(t) = A_{geo} \int_0^L i(x,t)\, dx \quad (9)$$

where A_{geo} [m^2] is the geometric surface area of the electrode. The corresponding voltage across the battery is given by:

$$V(t) = \phi_s^{avg}(x,t) - \phi_e^{avg}(x,t) - I(t) R_{int} \quad (10)$$

where R_{int} [Ω] is the internal resistance of the cell, and the potentials are spatially averaged over the electrode. The total energy output E [J] is obtained by integrating power over time:

$$E = \int_0^{t_{final}} I(t) V(t)\, dt \quad (11)$$

This theoretical framework describes the coupled effects of irradiation-induced defect dynamics, oxygen and lithium transport, Li_2O_2 precipitation, and electrochemical kinetics. It provides the basis to understand the biphasic behaviour observed in low compared with high irradiation doses. It explains both the enhancement of battery capacity at low doses and the collapse at excessive doses.

The closure of the model requires constitutive relations for transport and electrochemical activity under irradiation. Two functional forms were chosen: an exponential suppression of diffusivity with defect density, and a biphasic enhancement of reaction site density. Both are written explicitly in Eq. (7) and Eq. (8). Their selection is grounded in physical reasoning and supported by literature in radiation materials science. Equation (7) introduces an exponential decrease of diffusivity with defect density. This reflects the fact that defects act as scattering centers and traps for mobile species (Kreller *et al*., 2019; Koettgen *et al*., 2018). As the number of defects grows, the probability of a carrier moving without obstruction falls rapidly. The exponential form conveys this transition. It ensures that diffusivity is only weakly reduced at low defect concentrations, but decays strongly once a threshold density is crossed. This approach has been used to represent radiation-induced transport degradation in metals and oxides (Zupac *et al*., 1993; Rasmidi *et al*., 2021). The suppression factor, β, is not drawn from direct experimental data for lithium–air electrodes, since such data are not available. Instead, β was chosen as a parameter that sets the onset of suppression within the range of radiation-induced defect densities in solids.

Equation (8) defines a biphasic response of the active surface site density to defect concentration. At low defect levels, irradiation can roughen surfaces, introduce step edges, and expose new catalytic sites (Yan *et al*., 2021; Wandelt, 1991). These changes enhance reactivity and increase the available surface area. However, at high defect densities, clustering and blockage occur. Pores collapse, pathways are obstructed, and catalytic activity is lost. The biphasic functional form ensures that the surface area rises initially but falls once the density of defects becomes excessive. This type of behaviour has been reported in atomistic simulations and in experimental studies of irradiated alloys and catalysts (Meslin *et al*., 2013; Aidhy *et al*., 2015).

The amplitude factor A_{enh} was introduced to control the strength of the enhancement. It has no fixed experimental value but is selected within a physically reasonable range based on prior studies of irradiation-induced surface modification. To ensure that these choices were not arbitrary, a sensitivity analysis was carried out. Three parameters were varied systematically: the suppression factor β, the enhancement amplitude A_{enh}, and the defect recombination coefficient k_{rec}. The effect of β was to shift the point at which suppression becomes dominant. A larger β caused diffusivity to collapse at lower defect densities, while a smaller β delayed suppression. The effect of A_{enh} was to change the magnitude of

enhancement at low doses. Higher values produced a larger peak in reactivity, but the shape of the curve remained biphasic. The recombination coefficient k_{rec} influenced the steady-state defect density. Faster recombination reduced the accumulation of defects and widened the window in which enhancement was possible.

The results of the sensitivity analysis are presented in Figures 1a-c. The biphasic behaviour persists across all tested parameter values. The enhancement window shifts or changes magnitude, but the qualitative pattern is unchanged. This shows that the functional forms in Eqs. (7) and (8) are not artifacts of parameter choice. They reflect robust physical mechanisms and remain valid over a broad parameter space. Table 1 shows the key parameters used for the simulations in Figures 1a – c.

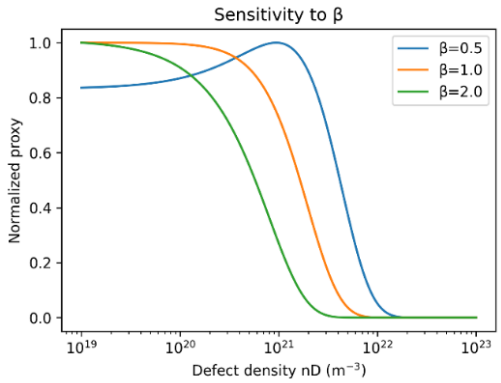

Figure 1a: Effect of suppression factor β on the normalized capacity proxy. Higher β narrows and shifts the enhancement window while retaining the biphasic trend.

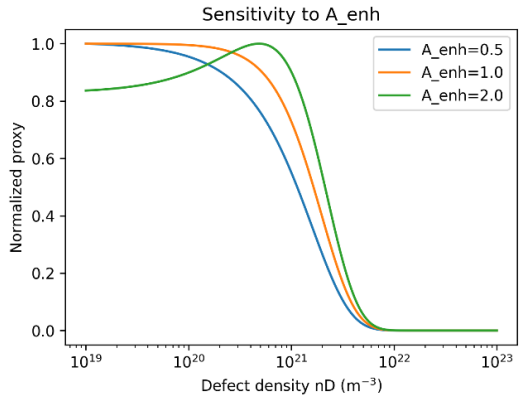

Figure 1b: Effect of amplitude enhancement factor A_{enh} on the normalized capacity proxy. Larger A_{enh} increases low-dose enhancement, with the biphasic pattern preserved.

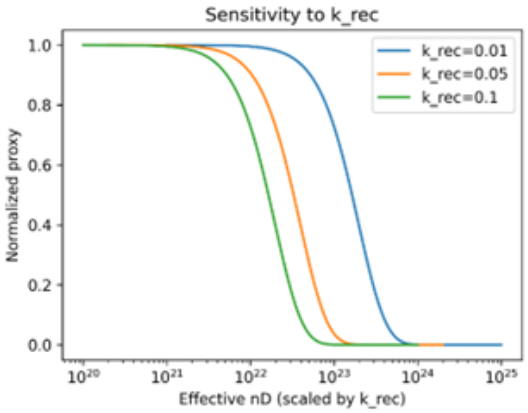

Figure 1c: Effect of recombination coefficient k_{rec} on the normalized capacity proxy. Scaling shifts the enhancement peak without altering the biphasic behaviour.

In summary, the exponential suppression law and the biphasic surface site law are justified on physical grounds. They are supported by radiation materials science and tested through sensitivity analysis. These laws are not fitted to direct experimental data for irradiated lithium–air batteries, since such data do not yet exist. However, they are grounded in well-established principles of irradiation damage and defect-mediated transport. The sensitivity study confirms that the model predictions are robust to variations in parameter choice.

2.2 Numerical Methods

The coupled electrochemical and defect evolution model was solved using a one-dimensional spatial discretization along the cathode thickness. The domain, representing the porous cathode, was divided into N uniform segments with spacing $\Delta x = L/(N-1)$, where L is the total electrode thickness. The model is solved in a one-dimensional cathode domain $0 \leq x \leq L$. At the electrode–electrolyte interface ($x = 0$), a fixed oxygen concentration boundary condition is imposed, while a zero-flux condition is applied at the current collector ($x = L$). For lithium, electroneutrality requires equal and opposite ionic fluxes at the two boundaries.

Table 1: Summary of key parameters utilized in producing the simulation results presented in Figures 1a–c

Category	Parameter	Symbol	Value(s)	Unit
Defect Density	Defect density sweep	n_D	1×10^{19} – 1×10^{23} (logspace)	m^{-3}
Material Constants	Base diffusivity	D_0	1×10^{-9}	$m^2 \cdot s^{-1}$
	Reference defect density	$n_{D,0}$	1×10^{21}	m^{-3}
	Max defect density	$n_{D,max}$	5×10^{22}	m^{-3}
	Baseline surface area	$a_{s,0}$	1.0	–
Sweep Parameters	Suppressor factors	β	[0.5, 1.0, 2.0]	–
	Enhancement factors	A_{enh}	[0.5, 1.0, 2.0]	–
	Recombination constants	k_{rec}	[0.01, 0.05, 0.1]	–

The electrolyte potential ϕ_e satisfies Ohm's law with a Dirichlet reference potential at $x = 0$. Initial conditions are uniform: oxygen and lithium concentrations are set to their baseline values: $C_{O_2}(x,0) = C_{O_{2,0}}$, $C_{Li}(x,0) = C_{Li,0}$, the defect density is initialized to a constant $n_D(x,0) = n_{D,0}$, and Li_2O_2 deposition is set to zero.

Spatial derivatives in the transport equations were approximated using second-order finite differences. It ensures accuracy while maintaining computational efficiency. Diffusion terms for oxygen and lithium were treated with variable coefficients to account for local defect-dependent diffusivity. A central difference scheme was applied for internal nodes. A one-sided difference was used at the boundaries to impose the fixed concentration conditions at the electrode–electrolyte interface. Time integration used an implicit solver designed for stiff systems of ordinary differential equations (ODE).

Stiffness came from the wide separation of time scales in the problem. Electrochemical reactions proceeded on very fast time scales. In contrast, diffusion and defect dynamics evolved at much slower rates. The backward differentiation formula (BDF) method was employed for time integration. This method ensured stability even when large time steps were used.

The partial differential equation (PDE) system was solved using second-order finite differences in space and BDF for stiff ODEs in time. The solver used was SciPy's BDF integrator (Python 3.12, SciPy 1.12). The cathode thickness was set to $L = 10^{-4}$ m and discretized into $N = 100$ nodes ($\Delta x = 1 \times 10^{-6}$ m). Relative tolerance = 10^{-6}, absolute tolerance = 10^{-9}, with adaptive time stepping and maximum $\Delta t = 0.01$ s. A complete model parameter table is shown in Tabel 2. To maintain accuracy, the solver was assigned both relative and absolute tolerances. These tolerances controlled numerical precision and reduced the risk of divergence caused by the strong nonlinearity of the Butler–Volmer kinetics.

The electrochemical current at each spatial node was computed using the full Butler–Volmer equation, which couples the local overpotential to the exchange current density. The exchange current itself was modulated by the defect-dependent biphasic enhancement factor. This approach accounted for the dose-dependent increase in reaction activity at moderate defect densities and the suppression at high densities.

Table 2: Numerical parameters used in the Lithium-air battery irradiation simulations

Symbol	Description	Value/Range	SI Unit	Source/Rationale
L	Cathode thickness	1.0×10^{-4}	m	Typical LAB porous cathode.
N	Number of grid points	100	-	Chosen for convergence.
Δx	Spatial step size	1.0×10^{-6}	m	Computed from L/N.
Δt_{max}	Maximum time step	1.0×10^{-2}	s	Chosen for stability.
$Rtol$	Relative tolerance	1.0×10^{-6}	-	Standard stiff ODE control.
$Atol$	Absolute tolerance	1.0×10^{-9}	-	Standard stiff ODE control.
$C_{O_{2,bulk}}$	Bulk oxygen concentration	1.0×10^{2}	$molm^{-3}$	Assumed, consistent with solubility estimates.
$D_{O_{2,0}}$	Oxygen diffusivity in pristine electrode	2.0×10^{-9}	m^2s^{-1}	Typical oxygen diffusivity in electrolyte.
D_{Li}	Lithium-ion diffusivity	1.0×10^{-10}	m^2s^{-1}	Value chosen to reflect moderate ionic transport consistent with porous electrode conditions.
$i_{0,0}$	Baseline exchange current density	1.0×10^{-5}	Am^{-2}	Estimated, adjusted for kinetics.
α_a, α_c	Anodic/cathodic transfer coefficient	0.5 each	-	Standard assumption.
F	Faraday constant	96485	$Cmol^{-1}$	Constant
T	Temperature	298	K	Room temperature
k_{precip}	Lithium peroxide precipitation rate constant	1.0×10^{3}	s^{-1}	Assumed, tuned for realistic lithium peroxide growth.
$n_{D,0}$	Reference defect density	1.0×10^{21}	m^{-3}	Scaling parameter.
$n_{D,max}$	Saturation defect density	5.0×10^{22}	m^{-3}	Suppression regime onset.
k_{rec}	Defect recombination coefficient	1.0×10^{-3}	s^{-1}	Assumed, typical for recombination.
D_D	Defect diffusion coefficient	1.0×10^{-14}	m^2s^{-1}	Chosen small to avoid localization.
β	Suppression factor	1.0	-	Tuning factor.
A_{enh}	Enhancement amplitude for surface area	2.0	-	Tuning factor.
$a_{s,0}$	Reference specific surface area	1.0×10^{5}	m^{-1}	Typical porous electrode.
A_{geo}	Geometric electrode surface area	1.0×10^{-4}	m^2	Electrode footprint.
R_{int}	Internal resistance	10	Ω	Estimated small cell resistance.
G	Defect generation rate (dose dependent)	10^{19}-10^{20}	$s^{-1}\ m^{-3}$	Varied across low, medium, high dose.

The local overpotential was calculated self-consistently by solving for the electrolyte potential, ϕ_e, using Ohm's law for ionic transport. The resulting linear system was updated at each time step. This ensured that the electrolyte potential showed the local current density. The calculation also accounted for the ionic conductivity, which decreases with increasing defect density.

Lithium peroxide, Li_2O_2 formation and chemical reactions were incorporated as source and sink terms in the mass balance equations. The

precipitation rate of Li_2O_2 was determined from the local lithium and oxygen concentrations. This rate was not constant but adjusted by the specific surface area, a_s. a_s changed over time because it evolved with the defect density.

Defect evolution was described within an advection–diffusion–reaction framework. In this approach, the generation of defects increased in proportion to the irradiation dose. Their loss occurred through recombination and annihilation, which were represented as a first-order decay process. A small diffusion term was included to prevent unphysical localization of defects at single grid points.

At each time step, the solver updated all state variables simultaneously. These included oxygen concentration, lithium concentration, Li_2O_2 deposition, defect density, and the electrolyte potential. The total current and voltage of the battery were then determined. This was done by integrating the local current density and by spatially averaging the potential across the electrode. Peak current and peak power were calculated from the time-dependent curves. Total capacity and total energy were obtained by integrating over the full discharge duration.

The simulation was repeated for different irradiation dose rates to investigate the full dose-dependent behaviour. Each case was initialized with the same baseline concentrations and defect density to allow direct comparison. The numerical method ensures that both transient and steady-state behaviour of the battery under irradiation are accurately resolved. It provides quantitative predictions of the enhancement or suppression of performance metrics.

2.3 Physical Plausibility of Defect Densities

The defect generation term G was explicitly linked to irradiation dose and dose rate.

For a particle flux φ [particles $m^{-2}.s^{-1}$] and displacement cross-section δ_d [m^2.particle^{-1}], the volumetric defect generation rate is: $G = \varphi \delta_d N_{atoms}$, where N_{atoms} is the number density of host atoms (m^{-3}). This formulation allows direct mapping of model "low/medium/high" dose regimes to experimental irradiation conditions. For example, with $\varphi = 10^{18}$ $m^{-2}.s^{-1}$, $\delta_d = 10^{-28}$ m^2, and $N_{atoms} = 8.5 \times 10^{28}$ m^{-3} (typical for nickel), $G \approx 8.5 \times 10^{19}$ $m^{-3}.s^{-1}$. The defect densities used in our simulations (10^{20} – 10^{22} m^{-3}) correspond to atomic fractions of about 10^{-8} – 10^{-6} relative to the host lattice. Such levels are consistent with experimentally reported defect populations in irradiated metals and oxides at doses ≤ 10^{-2} dpa (Was, 2007), where crystallinity and microstructural integrity are retained.

By comparison, catastrophic amorphization or swelling typically requires much higher defect densities, approaching 10^{25} m^{-3} (≈ 10^{-3} atomic fraction).

Experimental evidence further supports this range. In EUROFER97 steel irradiated to 15 – 32 dpa, dislocation-loop densities of ~ 1.4×10^{22} m^{-3} at 15 dpa and ~ 1.7×10^{22} m^{-3} at 32 dpa were reported without loss of overall microstructural integrity (Weiß *et al.*, 2012). In tungsten subjected to self-ion implantation, stable point-defect populations are also observed at doses well below the threshold for catastrophic structural failure (Reza *et al.*, 2020). These observations confirm that the defect densities assumed in our model are physically realistic and achievable without destroying the electrode microstructure.

2.4 Mass Conservation Validation

To verify the numerical consistency of our scheme, we tracked the sum of dissolved oxygen and solid Li_2O_2 over the full simulation. The initial total oxygen inventory was 1.60 a.u (arbitrary unit). Throughout the run, the maximum absolute deviation from this value was 2.22×10^{-16}. This corresponds to a relative deviation of 1.39×10^{-16}. Both deviations are within the solver tolerance. At the end of the simulation, the oxygen distribution was 1.5 a.u. in dissolved form and 0.1 a.u. in Li_2O_2, exactly conserving the total. This confirms that precipitation and transport processes are handled consistently. The scheme conserves mass to numerical precision (see Fig. 2).

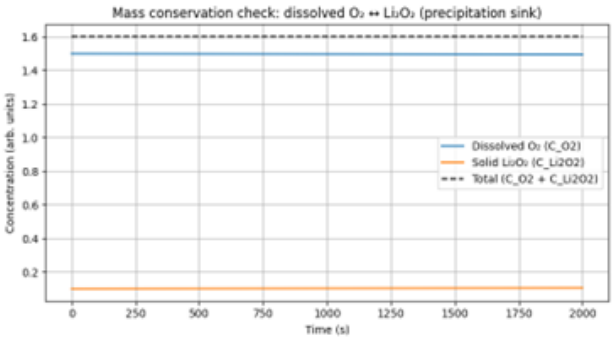

Figure 2: Mass conservation check showing total oxygen (O_2 + Li_2O_2) remains constant within solver tolerance. The key parameters for the simulation are: k_p = 1 x 10^{-5} m/s, a_s = 1.0 m^{-1}, C_{sat} = 1.0 mol.m^{-3}, n = 2.0, t_{final} = 2000.0 s, $C_{02,0}$ = 1.5 mol.m^{-3}, $C_{Li2O2,0}$ = 0.1 mol.m^{-3}.

2.5 Transport Model

We model oxygen as the dissolved species in the electrolyte that fills the porous cathode. Gas-phase transport and Knudsen effects are not solved as a separate field. They are instead lumped into an effective continuum diffusivity. The model uses the expression in eq. (7). This expression is a specific form of the common effective diffusivity:

$$D_{eff}(x.t) = \frac{\varepsilon}{\tau} D_l f_{supp}(n_D) \quad (12)$$

where ε represents the porosity, τ is the tortuosity, and D_l is the bulk liquid-phase oxygen diffusivity. The term $f_{supp}(n_D)$ describes the suppression of transport caused by defect buildup. In our model, the ratio $\frac{\varepsilon}{\tau}$ is absorbed into the baseline diffusivity $D_{O_{2,0}}$. The suppression function $f_{supp}(n_D)$ is implemented using the exponential dependence on defect density given in eq. (7).

Boundary coupling to the gas reservoir is treated by fixing the dissolved concentration at the electrode interface. This assumes rapid gas–liquid equilibration (Henry's law). Any interfacial mass-transfer resistance is therefore neglected in the present work. We note this approach is appropriate for electrolyte-flooded pores. If the electrode were dry or intentionally gas-filled, a two-phase gas and liquid model with explicit gas diffusion and Knudsen effects would be required. We set the baseline dissolved oxygen diffusivity to $D_{O_{2,0}} = 2\ x\ 10^{-9}\ m^2.s^{-1}$. This value lies within published ranges for common non-aqueous Li–air electrolytes (order 10^{-9} – 10^{-8} $m^2.s^{-1}$). See, for example, Gittleson et al. (2017) and Li et al. (2022). The lithium ion diffusivity is $D_{Li} = 1\ x\ 10^{-10}\ m^2.s^{-1}$. This is a standard bulk-electrolyte value reported in the literature. Porosity and tortuosity effects are incorporated by treating $D_{O_{2,0}}$ as an effective baseline. Irradiation effects are represented by the defect-dependent suppression term in eq. (7). In the present study we performed sensitivity tests on the irradiation-related parameters: the suppression factor, the defect recombination rate, and the surface-area enhancement amplitude. These sensitivity tests show the qualitative biphasic behaviour (low-dose enhancement, high-dose failure) is robust to changes in irradiation-coupling parameters..

3.0 Results and Discussion

The effect of irradiation dose on lithium–air battery performance was investigated by analyzing current, power, capacity, lithium peroxide profiles, electrolyte potential, and defect density. Figures 3 and 4 illustrate the temporal and spatial evolution of these quantities under control (non-irradiation condition), low-dose, medium-dose, and high-dose conditions. Figure 3a shows the current–time profiles. In the control case, the current remains weak and nearly flat, showing the slow kinetics of the non-irradiated cathode. At low dose, the current rises modestly and decays slowly, maintaining a sustained discharge over the simulated period. In contrast, the medium- and high-dose conditions exhibit sharp initial current spikes that exceed the control by nearly two hundred and four hundred percent, respectively. However, these enhancements are transient, and the current collapses quickly, leading to negligible long-term discharge. The power–time profiles in Figure 3b mirror the current behaviour.

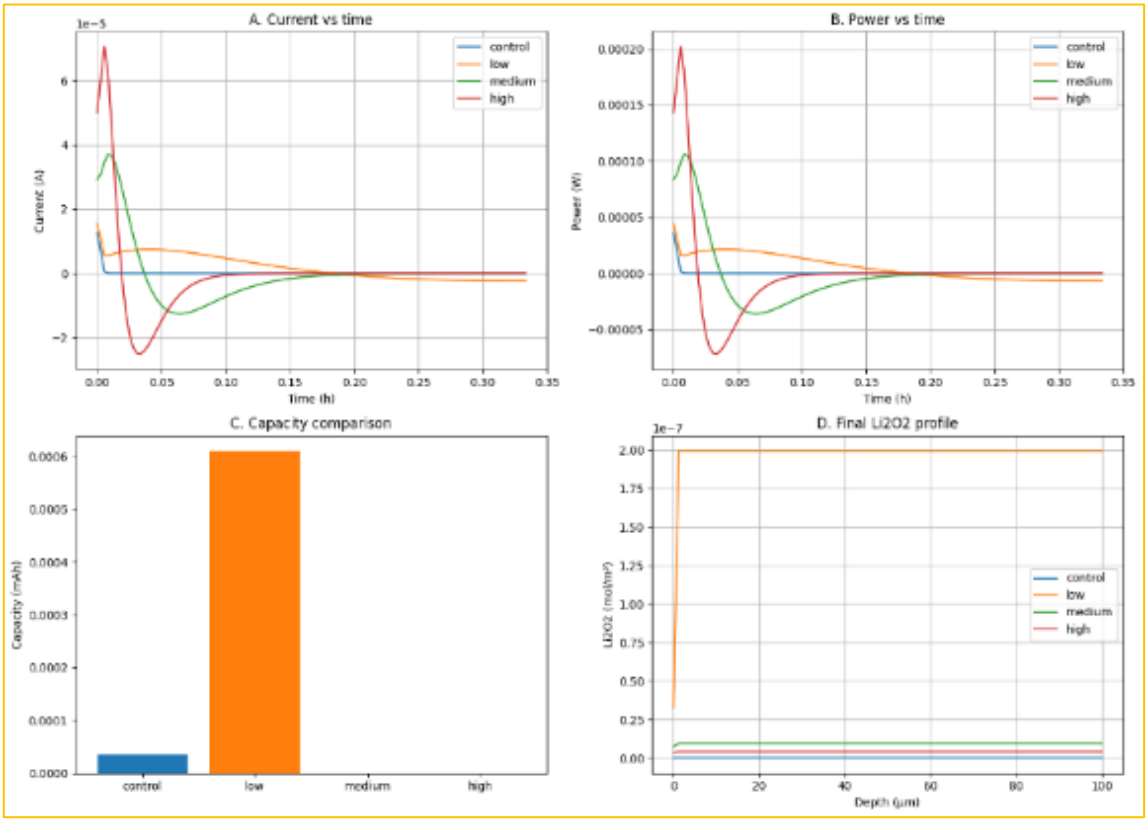

Figure 3: Electrochemical performance of the lithium–air battery under different irradiation conditions (control (non-irradiation condition), low dose, medium dose, and high dose). (A) Current–time profiles. (B) Power–time curves. (C) Capacity comparison. (D) Final Li_2O_2 deposition profiles across the cathode thickness. Simulation key parameters are reported in Table 3.

Control produces minimal power output. Low dose produces a stable increase in power, sustained throughout the discharge. Medium and high doses yield very large but short-lived power peaks. Quantitatively, medium dose reaches nearly 0.000106 W, while high dose exceeds 0.000202 W. These values represent increases of more than 190% and 460% compared with control. Yet, the integrated energy is negligible, confirming that transient spikes do not translate into usable performance.

The differences become clearer in the capacity comparison shown in Figure 3c. The control delivers a very small capacity of about 3.6×10^{-5} mAh. The low-dose case produces a dramatic enhancement, exceeding 6×10^{-4} mAh, which corresponds to more than fifteen hundred percent improvement relative to control. This enhancement reveals that a moderate level of irradiation-induced defects promotes charge transfer and effective utilization of the electrode. In stark contrast, both medium- and high-dose conditions deliver near-zero capacity despite their large instantaneous currents.

The lithium peroxide deposition profiles in Figure 3d provide further mechanistic insight. In the control case, Li_2O_2 accumulation is minimal, consistent with the very low current and capacity. Under low-dose irradiation, the profile shows uniform deposition across the electrode thickness, suggesting that transport remains effective and pore volume is utilized efficiently. For medium- and high-dose cases, however, the profiles are essentially flat near zero, indicating that the reactions terminate early and that no significant Li_2O_2 buildup occurs.

The electrochemical trends correlate strongly with the electrolyte potential behaviour. Figure 4a displays the evolution of the average

electrolyte potential during discharge. The control case remains almost constant at baseline levels. Low dose produces a small but stable rise. Medium dose initially increases but then levels off, indicating partial suppression of conductivity. At high dose, the potential rises sharply and diverges with time. This instability reflects the severe loss of ionic conductivity as defect density becomes excessive.

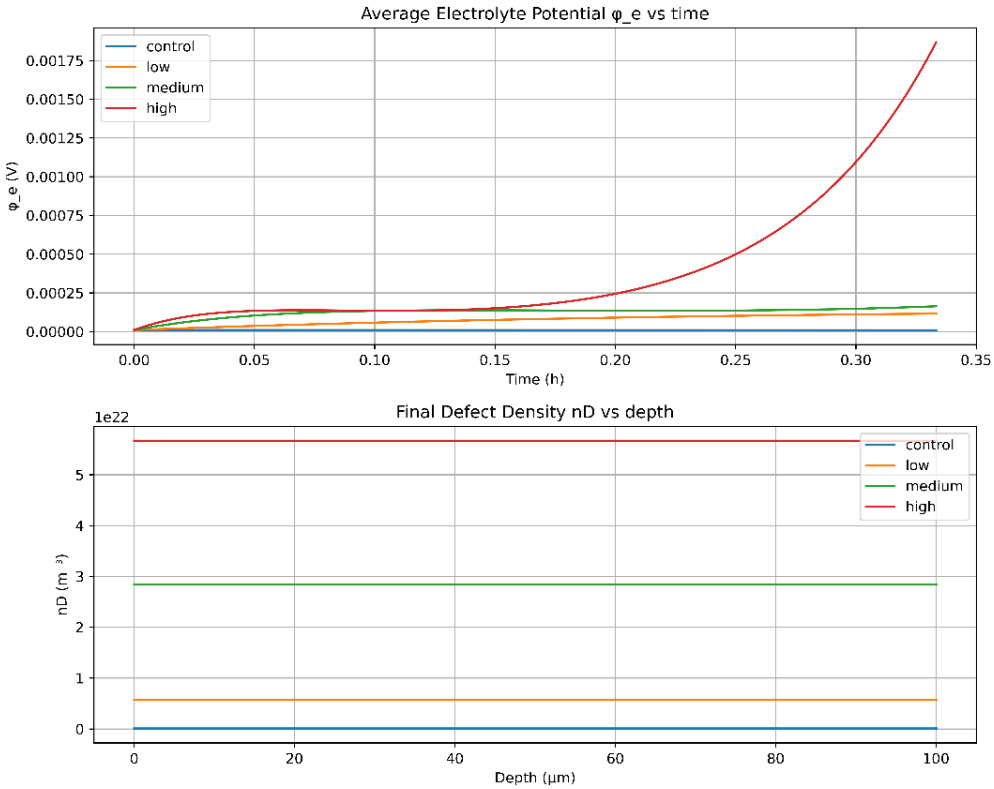

Figure 4: Electrolyte potential and defect density evolution under irradiation. (a) Average electrolyte potential-time profiles. (b) Final defect density profiles across electrode depth. The key parameters used for simulating these results are presented in Table 3.

The final defect density profiles in Figure 4b support the proposed biphasic mechanism. The control case shows no defect generation. At low dose, the defect density stabilizes near 10^{21} m^{-3}. According to the theoretical model, the benefit factor increases with defect density in the range 10^{20} –10^{21} m^{-3}, before exponential suppression dominates. This range therefore defines the enhancement window where defects promote electrochemical activity. The medium dose drives the concentration well above 10^{21} m^{-3}, while the high dose reaches values approaching 6×10^{22} m^{-3}. At such elevated levels, the exponential suppression of diffusivity and conductivity dominates. As a result, the beneficial enhancement observed at low dose is lost, leading to a complete collapse of both Li_2O_2 formation and battery capacity. Table 4 summarizes the peak current Ip, peak power Pp, capacity C, and energy E outcomes. At the control condition (non-irradiated battery), the electrochemical response is weak, with modest current, power, and energy values. At low irradiation dose, all metrics increase markedly: both current and power rise above the control, while capacity and energy show particularly large improvements in their absolute values. This indicates that mild irradiation enhances electrochemical activity and supports more extensive discharge. At very high irradiation doses, the model yields negative total energy values. Such outputs are not physically realizable. They signify a failure regime in which irradiation-induced defect accumulation suppresses electrochemical activity. In this regime, no usable energy can be extracted from

the battery. At medium and high doses, the discharge capacity collapses almost completely (0.0186 and 0.000135 × 10^{-5} mAh, respectively). This reflects severe blocking of Li_2O_2 growth pathways and oxygen transport. The behaviour is consistent with a transition to battery failure rather than normal operation.

Table 3: The key parameters employed in generating the simulation results presented in Figures 3 and 4

Category	Parameter	Symbol	Value	Unit
Physical Constants	Faraday constant	F	96,485.33	$C \cdot mol^{-1}$
	Gas constant	R	8.314	$J \cdot mol^{-1} \cdot K^{-1}$
	Temperature	T	298.15	K
System Geometry	Thickness	L	100×10^{-6}	m
	Grid points	N	80	–
	Grid spacing	Dx	1.27×10^{-6}	m
Electrochemical	O_2 diffusion coefficient	$D_{O_2,o}$	1.0×10^{-9}	$m^2 \cdot s^{-1}$
	Exchange current density	$i_{o,o}$	0.13	$A \cdot m^{-2}$
	Equilibrium potential	U_{eq}	2.96	V
	Internal resistance	R_{int}	5.0	Ω
	Geometric electrode area	A_{geo}	1.0×10^{-4}	m^2
Defect Parameters	Initial defect density	$n_{D,o}$	1.0×10^{20}	m^{-3}
	Enhancement coefficient	A_{enh}	0.5	–
	Saturation density	n_D*	5.0×10^{21}	m^{-3}
	Diffusion suppression	β	0.001	–
	Exchange suppression	Γ	0.02	–
	Surface suppression	Z	0.1	–
	Baseline surface area	$a_{s,o}$	1.0×10^5	m^{-1}
Kinetics	Charge-transfer factor	α_a	0.5	–
	Charge-transfer factor	α_c	0.5	–
	Chemical reaction rate	k_{chem}	1.0×10^3	–
	Precipitation rate	k_{precip}	1.0×10^2	–
Simulation Setup	Final time	t_{final}	1200	s

	Evaluation points	t_{eval}	120	–
	Atom density	N_{atoms}	5.0×10^{28}	m^{-3}
Dose Cases	Control	G	0.0	$m^{-3}\cdot s^{-1}$
	Low	G	5.0×10^{18}	$m^{-3}\cdot s^{-1}$
	Medium	G	2.5×10^{19}	$m^{-3}\cdot s^{-1}$
	High	G	5.0×10^{19}	$m^{-3}\cdot s^{-1}$

Table 4: Simulated electrochemical performance parameters of lithium–air batteries under different irradiation doses

Dose	I_P [10^{-5}A]	P_p [10^{-5}W]	C [10^{-5} mAh]	E [10^{-5} J]
Control	1.30	3.60	3.60	36.9
Low	1.50	4.40	60.9	627
Medium	3.70	10.6	0.0186	0.133
High	7.10	20.2	0.000135	-0.110

Equation (13) defines the percentage enhancement formula, where $I_{P,dose}$, $P_{P,dose}$, $E_{P,dose}$ are the peak current, peak power, and total energy at a given irradiation dose. The terms $I_{control}$, $P_{control}$, $E_{control}$ are the corresponding values in the non-irradiated control. Here, X can represent current (I), power (P), or energy (E).

$$\% \Delta X = \frac{X_{P,dose} - X_{control}}{X_{control}} x\ 100\% \quad (13)$$

The values presented in Table 5 are obtained by applying Eq. (13) to the results in Table 4. At low irradiation dose, the peak current and peak power increase by 15% and 22% relative to the control. Capacity and energy show dramatic gains of more than fifteen hundred percent. This suggests that mild irradiation introduces beneficial defect states. These defects enhance active sites and oxygen transport, thereby boosting electrochemical kinetics.

Table 5: Percentage enhancement relative to control across all irradiation doses

Dose	**%Δ*I***	**%Δ*P***	**%Δ*C***	**%Δ*E***
Control	0.0	0.0	0.0	0.0
Low	15.4	22.2	1.59×10^3	1.60×10^3
Medium	185	194	-99.5	-99.6
High	446	461	-100.	-100.

At medium and high doses, the apparent current and power continue to rise, showing 185% and 446% increase, respectively. However, both capacity and energy fall sharply to –100% relative to the control. This indicates a failure regime in which excessive irradiation produces defect densities that block Li_2O_2 growth pathways and suppress discharge. The result is zero usable capacity and energy.

Taken together, these results reveal a biphasic irradiation effect. Moderate irradiation enhances battery performance. In contrast, excessive irradiation causes severe degradation and ultimately leads to electrochemical failure.

Figure 5 presents bar charts showing the percentage enhancement of key performance metrics relative to the control case under different irradiation doses. The results highlight the dose-dependent response of the system, where irradiation modifies current, power, capacity, and energy in distinct ways. At lower doses, enhancements are moderate and reflect improved defect-assisted transport, while at higher doses the trends indicate the onset of limiting behaviour.

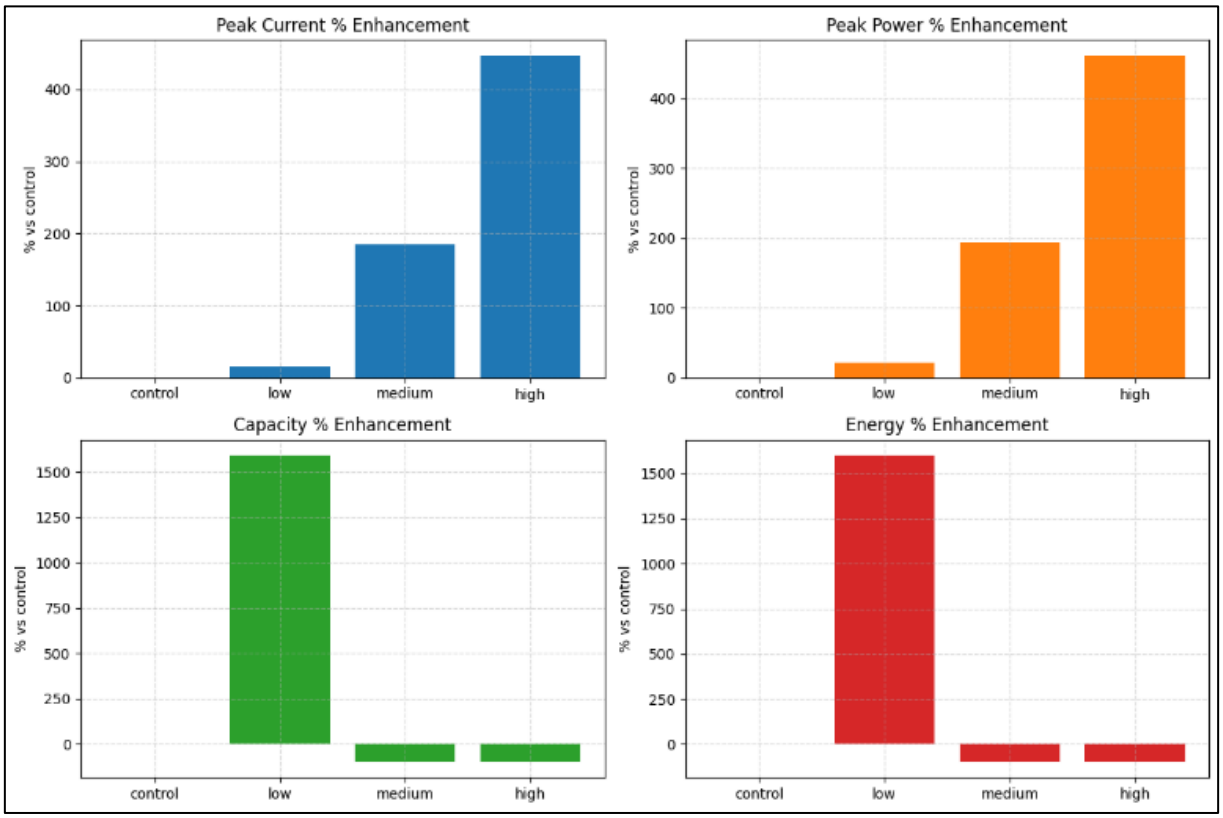

Figure 5: Bar charts of (a) Peak current enhancement, (b) Peak power enhancement, (c) Capacity enhancement, and (d) Energy enhancement.

The bar charts in Figure 5 illustrate the trends in percentage enhancement of the performance metrics shown in Table 5. Overall, the results establish a dose-dependent response that is highly nonlinear. Low-dose irradiation improves kinetics, reaction uniformity, and product formation. Medium and high doses drive the system beyond its optimal defect window, causing catastrophic suppression of transport and early reaction termination. The interplay of Figures 1, 3, 4, and 5 with Tables 4 and 5 confirm that irradiation is a "double-edged sword": beneficial at low levels but detrimental when excessive.

3.1 Validation and Physical Realism

To assess the plausibility of the model predictions, we compared our results with trends reported in related irradiated electrochemical systems. Direct experimental studies of Li–air batteries under irradiation are not available to the best of our knowledge. However, reports on irradiated Li-ion and solid-state batteries indicate that irradiation can significantly enhance ionic mobility (Gao *et al*., 2023; Qiu *et al*., 2015). It can also alter electrode/electrolyte interfacial kinetics (Tan et al., 2016; Yu *et al*., 2025). These effects can lead to substantial capacity increases under certain conditions.

Our predicted large percentage changes—for example, a capacity exceeding 1500% at low irradiation dose—are consistent in direction with reported trends. Although no experimental data confirm capacity increases of this magnitude in irradiated lithium-ion batteries, there are reports of enhanced capacity at low irradiation doses (Nam *et al*., 2025; Lee *et al*., 2019). However, the exact percentage increase is not explicitly stated.

To further ensure physical realism, we carried out a limiting-case test by setting both the suppression factor (β) and defect generation rate (G) to zero, effectively eliminating irradiation-induced defects. Under this condition, the model output reverts to the control (non-irradiated) case, with peak current, capacity, and total energy nearly identical to baseline values (Table 6). This confirms that the model produces

physically consistent behaviour in the absence of irradiation effects. Table 7 presents the key parameters employed to produce the results reported in Table 6.

Together, these two lines of analysis - qualitative consistency with experimental expectations in related systems and the limiting-case validation support the plausibility of our predictions.

Table 6: Comparison of peak current (I_P), capacity (C), and total energy (E) between the control case and the limiting-case test ($\beta = 0$, $G = 0$)

Case	I_p **[10^{-6} A]**	C **[10^{-5} mAh]**	E **[10^{-4} J]**
Control	4.586	1.061	1.092
Limiting	4.586	1.058	1.089

Table 7: Summary of key parameters utilized in generating the simulation data shown in Table 6

Category	Parameter	Symbol	Value	Unit
Geometry	Electrode thickness	L	1.0×10^{-4}	m
	Number of grid points	N	40	–
	Grid spacing	Dx	computed from L and N	m
Simulation	Final time	t_{final}	600.0	s
	Evaluation points	t_{eval}	80	–
Electrochemical	O_2 diffusivity	$D_{O2,0}$	1.0×10^{-9}	$m^2 \cdot s^{-1}$
	Exchange current density	$i_{0,0}$	13×10^{-2}	$A \cdot m^{-2}$
	Equilibrium potential	U_{eq}	2.96	V
	Fixed activation overpotential	$\boldsymbol{\eta}$	0.1	V
	Faraday constant	F	96485.3329	$C \cdot mol^{-1}$
	Geometric electrode area	A_{geo}	1.0×10^{-4}	m^2
Reaction	Chemical reaction rate	k_{chem}	1.0×10^{3}	–
	Precipitation rate	k_{precip}	1.0×10^{2}	–
	Baseline surface area	$a_{s,0}$	1.0×10^{5}	m^{-1}
Model	Defect density reference	$n_{D,0}$	1.0×10^{20}	m^{-3}
	Kinetic parameter ζ	Z	10^{-3} (control) / 0.0 (limiting)	–
	Kinetic parameter γ	Γ	0.05 (control) / 0.0 (limiting)	–
	Surface suppression β	β	0.1 (control) / 0.0 (limiting)	–
	Defect generation rate	G	0.0	$m^{-3} \cdot s^{-1}$

They also highlight the need for future dedicated experimental work on irradiated Li–air battery systems to confirm these trends.

3.2 Electrolyte Potential Profiles under Varying Irradiation Dose Rates and Mesh Resolutions

The electrolyte potential was evaluated across the electrode for different defect generation rates, G, and mesh resolutions, N as shown in Figure 6. At moderate defect densities, the curves for $N = 50$, 100, and 200 overlap closely. This indicates numerical convergence and mesh independence in the pre-collapse regime. This confirms that the discretization and solver settings are adequate to describe the system's behaviour before divergence.

As the local defect density approaches its maximum, the electrolyte potential rises sharply. This shows a physical blow-up caused by severely reduced ionic conductivity. The reduction effectively limits ionic transport. This divergence occurs consistently across different meshes. This confirms that it is a physical phenomenon rather than a numerical artifact. Higher defect generation rates shift the onset of this divergence toward lower positions. This demonstrates that increased irradiation accelerates the approach to the collapse regime. In contrast, lower rates maintain finite potential across most of the domain. These observations suggest that regions of sharp potential increase correspond to severely hindered ionic transport and potential localized performance failure. In contrast, the pre-collapse region represents stable and physically meaningful electrochemical behaviour.

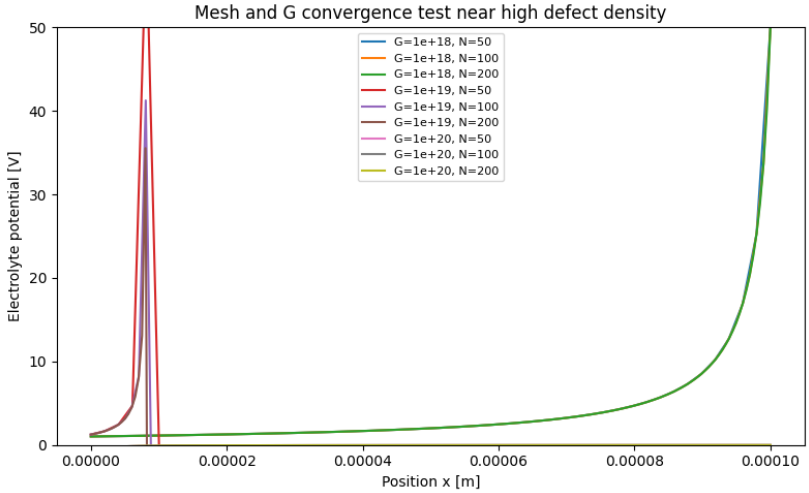

Figure 6: Electrolyte potential profiles showing mesh convergence at moderate densities and irradiation-driven divergence at high defects. The simulation key parameters for these results are: $L = 10^{-4}$ m; mesh resolution (N) = 50, 100, 200; $G = 1 \times 10^{18}$ $m^{-3}s^{-1}$, 1×10^{19} $m^{-3}s^{-1}$, 1×10^{20} $m^{-3}s^{-1}$; and $n_{D,max} = 5 \times 10^{22}$ m^{-3}.

3.3. Transient Current Spike Analysis

To investigate the transient electrochemical events in the system, we analyzed a simulated current spike using a fine temporal resolution. The multi-panel figure (Figure 7) illustrates the current, integrated charge, reaction source terms, and a zoomed-in view of the spike. This approach allows assessment of the physical significance of short-lived reaction events.

(a) Time-integrated current (capacity):

The first panel of Figure 7 shows the transient current spike over time. The current rises sharply to a peak of $\sim 1 \times 10^{-5}$ A around $t = 0.5$ s. It then rapidly decays back to near zero within a narrow time window. This indicates a sudden, localized electrochemical event rather than a sustained reaction. The integrated charge (second panel) increases only while the current is nonzero. It reaches a plateau immediately after the spike. The total integrated charge is $Q_{spike} \approx 2.51 \times 10^{-6}$ C ($\approx 6.97 \times 10^{-7}$ mAh). This corresponds to $n \approx 2.6 \times 10^{-11}$ mol e^-. After the spike, the integrated

charge remains constant. This confirms that the transient current does not contribute to lasting Li_2O_2 formation.

(b) Local reaction source terms:

The third panel of Figure 7 plots the reaction rate ($R = I/F$) as a function of time. The reaction rate rises with the current. It peaks at $t \approx 0.5$ s at $\sim 1.04 \times 10^{-10}$ mol/s. It then decays back to near zero within ~ 0.5 s after the peak. The spike is strictly confined to a narrow time window. This shows that the chemical transformation is transient and does not accumulate afterward. This confirms the absence of spurious displacement currents. It also demonstrates that the source term evolution is physically consistent with the governing electrochemical equations.

(c) Time-step refinement check:

The bottom panel of Figure 7 provides a zoomed-in view around the peak (0.4–0.6 s). It shows the fine-resolution reaction rate. The spike rises and falls symmetrically. The integrated charge during this interval accounts for virtually all of the total reaction extent. This demonstrates that the spike is fully resolved numerically. It confirms the physical validity of the transient event.

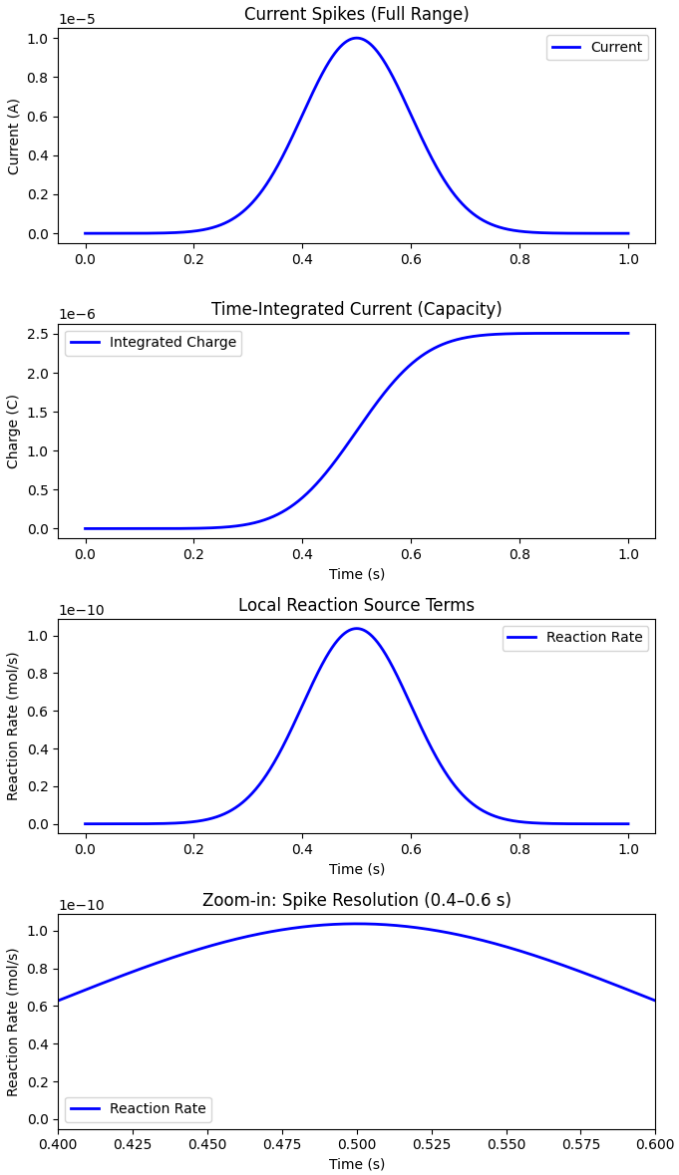

Figure 7: Multi-panel illustration of transient current spike analysis. (a) Current spike profile. (b) Time-Integrated current (capacity) profile. (c) Local reaction source terms profile. (d) Current spike resolution profile.

4.0 Conclusion

This study developed and applied a coupled electrochemical–defect evolution model to investigate the effects of irradiation dose on lithium–air battery performance. The theoretical framework accounted for oxygen and lithium transport, lithium peroxide formation, and full Butler–Volmer electrochemical kinetics. All of these processes were modulated by irradiation-induced defects. Defect density was treated as a dynamic variable. It increased with dose and evolved through recombination and migration. Its influence on transport and kinetics was explained through a biphasic enhancement factor for reaction activity and an exponential suppression of diffusivity and conductivity. This formulation predicted a narrow window of beneficial defect densities where battery performance improves. It also predicted destructive suppression beyond this threshold.

Numerical simulations confirmed the model predictions. The control case produced minimal current, power, and capacity. This reflected slow reaction kinetics in the absence of irradiation. Low-dose irradiation enhanced the exchange current density and reaction surface area without severely impeding transport. As a result, current and power increased by modest amounts. Capacity and energy rose by more than fifteen hundred percent compared with control. This demonstrates the constructive role of defects when confined to the enhancement window.

At medium and high irradiation doses, the response changed dramatically. Large spikes in peak current and power were observed. However, they were short-lived and unsustainable. The corresponding discharge capacity and energy were nearly zero. Lithium peroxide deposition profiles confirmed the absence of significant product growth. The electrolyte potential diverged as ionic conductivity collapsed. The final defect density exceeded the theoretical enhancement window, reaching values above $10^{22}\,m^{-3}$. In this regime, exponential suppression of transport overwhelmed any kinetic gains. This led to complete performance failure. The combined evidence from Figures 1, 3, 4, and 5 and Tables 4 and 5 establishes irradiation as a double-edged influence on lithium–air batteries. At low dose, irradiation-induced defects enhance reaction kinetics and enable uniform product formation. This boosts overall performance. At higher doses, however, the same defects accumulate beyond the optimal threshold. They produce catastrophic transport suppression and battery collapse. This biphasic response reveals the critical importance of defect management in irradiated electrochemical systems.

References

Aidhy, D. S., Lu, C., Jin, K., Bei, H., Zhang, Y., Wang, L., & Weber, W. J. (2015). Point defect evolution in Ni, NiFe and NiCr alloys from atomistic simulations and irradiation experiments. *Acta Materialia*, *99*, 69-76. https://doi.org/10.1016/j.actamat.2015.08.007.

Akhtar, N., & Akhtar, W. (2015). Prospects, challenges, and latest developments in lithium–air batteries. *International Journal of Energy Research, 39*(3), 303-316. https://doi.org/10.1002/er.3230.

Akintunde, S. O., & Selyshchev, P. A. (2016). The influence of radiation-induced vacancy on the formation of thin-film of compound layer during a reactive diffusion process. *Journal of Physics and Chemistry of Solids, 92*, 64-69. https://doi.org/10.1016/j.jpcs.2016.01.020.

[a]Akintunde, S. O., Selyshchev, P. A., & Kehinde, D. O. (2025). Growth Kinetics of Refractory Metal Silicide under Radiation Induced Interstitial Mechanism: An Analytical Approach. *BIMA Journal of Science and Technology (2536-6041), 9*(1B), 274-282. https://journals.gjbe-academia.com/index.php/bimajst/article/view/958.

[b]Akintunde, S. O., Selyshchev, P. A., & Kehinde, D. O. (2025). Temperature Variation in an AB Bilayer System During Radiation-Induced AB Compound Layer Formation. *FUDMA Journal of Sciences, 9*(2), 98-104. https://doi.org/10.33003/fjs-2025-0902-3144.

Amine, K., Kanno, R., & Tzeng, Y. (2014). Rechargeable lithium batteries and beyond: Progress, challenges, and future directions. *Mrs Bulletin, 39*(5), 395-401. https://doi.org/10.1557/mrs.2014.62.

Bugga, R., Smart, M., Whitacre, J., & West, W. (2007, March). Lithium-ion batteries for space applications. In *2007 IEEE Aerospace Conference* (pp. 1-7). IEEE. https://doi.org/10.1109/AERO.2007.352728.

Chowdhury, S. R. (Ed.). (2022). *Radiation technologies and applications in materials science*. CRC Press. ISBN: 9781000807233.

Fan, Y. (2025). Atomistic Modeling of Microstructural Defect Evolution in Alloys Under Irradiation: A Comprehensive Review. *Applied Sciences, 15*(16), 9110. https://doi.org/10.3390/app15169110.

Gao, Y., Qiao, F., Hou, W., Ma, L., Li, N., Shen, C., ... & Xie, K. (2023). Radiation effects on lithium metal batteries. *The Innovation, 4*(4). https://doi.org/10.1016/j.xinn.2023.-100468.

Gittleson, F. S., Jones, R. E., Ward, D. K., & Foster, M. E. (2017). Oxygen solubility and transport in Li–air battery electrolytes: establishing criteria and strategies for electrolyte design. *Energy & Environmental Science*, *10*(5), 1167-1179. https://-doi.org/10.1039/C6EE02915A.

Guo, J., Meng, X., Wang, Q., Zhang, Y., Yan, S., & Luo, S. (2024). Advancements in Lithium - Oxygen Batteries: A Comprehensive Review of Cathode and Anode Materials. *Batteries, 10*(8), 260. https:/-/doi.org/10.3390/batteries10080260.

He, Y., Chen, Z., & Zhang, Y. (2024). Strategies for improving cathode electrolyte interphase in high-performance dual-ion batteries. *Iscience, 27*(8). https://doi.org/-10.1016/j.isci.2024.110491.

Huang, X., Li, M., Gao, Y., Park, M. G., Matsuda, S., & Amine, K. (2025). Discharge Rate-Driven Li2O2 Growth Exhibits Unconventional Morphology Trends in Solid-State Li-O2 Batteries. *Angewandte Chemie International Edition, 64*(37), e202507967. https://-doi.org/10.1002/anie.202507967.

Imanishi, N., Luntz, A. C., & Bruce, P. (Eds.). (2014). *The lithium air battery: fundamentals* (pp. 1-21). New York: Springer. https://doi.org/10.1007/978-1-4899-8062-5.

Khan, M. H., Tucci, V., Lamberti, P., Longo, R., & Guadagno, L. (2025). Lithium-Based Batteries in Aircraft. *Engineering Proceedings, 90*(1), 39. https://doi.org/-10.3390/engproc2025090039.

Koettgen, J., Grieshammer, S., Hein, P., Grope, B. O., Nakayama, M., & Martin, M. (2018). Understanding the ionic conductivity maximum in doped ceria: trapping and blocking. *Physical Chemistry Chemical Physics*, *20*(21), 14291-14321. https://doi.org/10.1039-/C7CP08535D.

Kreller, C. R., Valdez, J. A., Holesinger, T. G., Morgan, J., Wang, Y., Tang, M., ... & Uberuaga, B. P. (2019). Massively enhanced ionic transport in irradiated crystalline pyrochlore. *Journal of Materials Chemistry A*, *7*(8), 3917-3923. https://doi.org/10.1039/C8TA10967B.

Kulathuvayal, A. S., & Su, Y. (2023). Ionic transport through the solid electrolyte interphase in lithium-ion batteries: A

review from first - principles perspectives. *ACS Applied Energy Materials, 6*(11), 5628-5645. https://doi.org/10.1021/-acsaem.3c00287.

Lampic, G., Gotovac, G., Geaney, H., & O'Dwyer, C. (2016). Comparing the suitability of Lithium ion, Lithium Sulfur and Lithium air batteries for current and future vehicular applications. *arXiv preprint arXiv:1606.06347*. https://-doi.org/10.48550/arXiv.1606.06347.

Lee, A., Vörös, M., Dose, W. M., Niklas, J., Poluektov, O., Schaller, R. D., ... & Johnson, C. S. (2019). Photo-accelerated fast charging of lithium-ion batteries. *Nature Communications*, *10*(1), 4946. https://doi.org/10.1038/s41467-019-12863-6.

Li, Q., Zhang, T., Zhang, T., Xue, Z., & Sun, H. (2022). Study on two-phase permeation of oxygen and electrolyte in lithium air battery electrode based on digital twin. *Energies*, *15*(19), 6986. https://doi.-org/10.3390/en15196986.

Liu, T., Vivek, J. P., Zhao, E. W., Lei, J., Garcia-Araez, N., & Grey, C. P. (2020). Current challenges and routes forward for nonaqueous lithium – air batteries. *Chemical Reviews, 120*(14), 6558-6625. https://doi.org/10.1021/acs.chemrev.9b00545.

Liu, X., Song, X., Zhang, Q., Zhu, X., Han, Q., Liu, Z., ... & Zhao, Y. (2022). Decomposition pathway and stabilization of ether-based electrolytes in the discharge process of Li-O2 battery. *Journal of Energy Chemistry, 69*, 516-523. https://doi.org/10.1016/j.jechem.2022.01.007.

Lüchtefeld, J., Lee, M. Y., Hemmelmann, H., Wachs, S., Behling, C., Mayrhofer, K. J., ... & Berkes, B. B. (2023). Contribution of electrolyte decomposition products and the effect of temperature on the dissolution of transition metals from cathode materials. *ACS Omega, 8*(36), 32606-32614. https://doi.org/10.1021/acsomega.3c03173.

Mbayachi, V. B. (2025). Ionic transport mechanisms in inorganic solid electrolytes: Interface, NMR and DNP studies. *Next Materials, 8*, 100657. https://doi.org/-10.1016/j.nxmate.2025.100657.

Meslin, E., Radiguet, B., & Loyer-Prost, M. (2013). Radiation-induced precipitation in a ferritic model alloy: An experimental and theoretical study. *Acta Materialia*, *61*(16), 6246-6254. https://doi.org/10.1016/-j.actamat.2013.07.008.

Nam, D., Moon, J. H., Jin, Y., Seong, H., Choi, B. E., Na, C. W., ... & Choi, J. (2025). Exploring enhanced capacity in lithium-ion battery anodes: Synthesis and electrochemical evaluation of Zn2GeO4 encapsulated in porous carbon balls via carbonization. *Journal of Energy Storage*, *107*, 114858. https://doi.org/-10.1016/j.est.2024.114858.

Numan-Al-Mobin, A. M., Schmidt, B., Lannerd, A., Viste, M., Qiao, Q., & Smirnova, (2022). Interdigitated cathode–electrolyte architectural design for fast-charging lithium metal battery with lithium oxyhalide solid-state electrolyte. *Materials Advances, 3*(24), 8947-8957. https://-doi.org/10.1039/D2MA00512C.

Qiu, J., He, D., Sun, M., Li, S., Wen, C., Hattrick-Simpers, J., ... & Cao, L. (2015). Effects of neutron and gamma radiation on lithium-ion batteries. *Nuclear Instruments and Methods in Physics Research Section B: Beam Interactions with Materials and Atoms, 345*, 27-32. https://doi.org/-10.1016/j.nimb.2014.12.058.

Rahman, M. A., Wang, X., & Wen, C. (2013). High energy density metal-air batteries: a

review. *Journal of the Electrochemical Society, 160*(10), A1759. DOI 10.1149-/2.062310jes.

Rasmidi, R., Duinong, M., & Chee, F. P. (2021). Radiation damage effects on zinc oxide (ZnO) based semiconductor devices–a review. *Radiation Physics and Chemistry*, *184*, 109455. https://doi.org/-10.1016/j.radphyschem.2021.109455.

Reza, A., Yu, H., Mizohata, K., & Hofmann, F. (2020). Thermal diffusivity degradation and point defect density in self-ion implanted tungsten. *Acta Materialia*, *193*, 270-279. https://doi.org/10.48550-/arXiv.1909.13612.

Tan, C., Lyons, D. J., Pan, K., Leung, K. Y., Chuirazzi, W. C., Canova, M., ... & Cao, L. R. (2016). Radiation effects on the electrode and electrolyte of a lithium-ion battery. *Journal of Power Sources, 318*, 242-250. https://doi.org/10.1016-/j.jpowsour.2016.04.015.

Wandelt, K. (1991). Properties and influence of surface defects. *Surface science*, *251*, 387-395. https://doi.org/10.1016/0039-6028-(91)91021-O.

Was, G. S. (2007). *Fundamentals of radiation materials science: metals and alloys.* Berlin, Heidelberg: Springer Berlin Heidelberg. https://doi.org/10.1007/978-3-540-49472-0_8.

Weiß, O. J., Gaganidze, E., & Aktaa, J. (2012). Quantitative characterization of microstructural defects in up to 32 dpa neutron irradiated EUROFER97. *Journal of nuclear materials*, *426*(1-3), 52-58. https://doi.org/10.1016/j.jnucmat.2012.03.027.

Yan, X., Zhuang, L., Zhu, Z., & Yao, X. (2021). Defect engineering and characterization of active sites for efficient electrocatalysis. *Nanoscale*, *13*(6), 3327-3345. https://doi.org/10.1039/-D0NR08976A.

Yu, M., Liu, Q., Rao, Y., Wang, H., Liu, P., Li, X., ... & Fang, S. (2025). High energy electron beam irradiation on the electrolyte enables fast-charging of lithium metal batteries with long-term cycling stability. *Physical Chemistry Chemical Physics, 27*(12), 6064-6071. https://doi.org/-10.1039/D5CP00021A.

Zaidi, S. S. H., & Li, X. (2023). Li–O2/air batteries using ionic liquids – a comprehensive review. *Advanced Energy Materials, 13*(28), 2300985. https://doi.-org/10.1002/aenm.202300985.

Zhang, X., Hattar, K., Chen, Y., Shao, L., Li, J., Sun, C., ... & Nastasi, M. (2018). Radiation damage in nanostructured materials. *Progress in Materials Science, 96*, 217-321. https://doi.org/10.1016/j.pmatsci-.2018.03.002.

Zupac, D., Galloway, K. F., Schrimpf, R. D., & Augier, P. (1993). Radiation-induced mobility degradation in p-channel double-diffused metal - oxide-semiconductor power transistors at 300 and 77 K. *Journal of applied physics*, *73*(6), 2910-2915. https://doi.org/10.1063/1.353021